AGU PUBLICATIONS

Geophysical Research Letters

RESEARCH LETTER

10.1002/2016GL070253

Key Points:

- First characterization of the primary modes of variability of E region, height-dependent conductivities over the entire polar region
- Three-dimensional modes reveal the particle precipitation-controlled conductivity responses to IMF Bz and Poynting flux
- Two-dimensional and 3-D representations of conductivity variability are distinctly different

Supporting Information:

- Supporting Information S1
- Figure S1
- Figure S2
- Figure S3

Correspondence to:
R. McGranaghan,
ryan.mcgranaghan@colorado.edu

Citation:
McGranaghan, R., D. J. Knipp, and T. Matsuo (2016), High-latitude ionospheric conductivity variability in three dimensions, *Geophys. Res. Lett.*, *43*, 7867–7877, doi:10.1002/2016GL070253.

Received 30 JUN 2016
Accepted 27 JUL 2016
Accepted article online 1 AUG 2016
Published online 14 AUG 2016

High-latitude ionospheric conductivity variability in three dimensions

Ryan McGranaghan[1], Delores J. Knipp[1,2], and Tomoko Matsuo[3,4]

[1]Aerospace Engineering Sciences, University of Colorado Boulder, Boulder, Colorado, USA, [2]High Altitude Observatory, National Center for Atmospheric Research, Boulder, Colorado, USA, [3]Cooperative Institute for Research in Environmental Sciences, Boulder, Colorado, USA, [4]National Oceanic and Atmospheric Administration, Boulder, Colorado, USA

Abstract We perform the first ever global-scale, altitude-dependent analysis of polar ionospheric conductivity variability using spectrally resolved in situ satellite particle measurements. With an empirical orthogonal function analysis we identify three primary modes of three-dimensional variability related to ionospheric footprints of the quiet and disturbed geospace environment: (1) perturbation of the quasi-permanent auroral oval, (2) differing projections of electron precipitation during southward and northward interplanetary magnetic field, and (3) a likely imprint of variation in Alfvénic Poynting flux deposition. Together, these modes account for >50% of the total conductivity variability throughout the *E* region ionosphere. Our results show that height-integrated conductance and height-dependent conductivities are distinctly different, underscoring the importance of studying the ionosphere in three dimensions. We provide the framework for future three-dimensional global analysis of ionosphere-magnetosphere coupling.

1. Introduction

Amm et al. [2008] identified global height profiles of ionospheric conductivities as the critical information needed to support auroral ionospheric electrodynamics analyses and data assimilation. Due to lack of observation, it has been impractical, if not impossible, to acquire the three-dimensional (3-D) structure of the conductivity globally [*Lilensten et al.*, 1997, and references therein]. There has been some recent progress in volumetric estimates of 3-D conductivity. *Semeter et al.* [2009] presented the first results from a fully 3-D regional volumetric imaging of the ionosphere via Poker Flat Incoherent Scatter Radar. *Lynch and Hampton* [2015] studied the 3-D structure and dynamics of field-aligned currents in auroral arcs using data collected from a sounding rocket together with larger-scale, contextual measurements from several ground-based instruments. Nonetheless, until now global quantification of 3-D conductivity has not been available.

Conductivity profiles are strongly modulated by the energy distribution of particles precipitating from the magnetosphere. *Newell et al.* [2009] explored the precipitation characteristics of magnetospheric electrons and showed that different energy distributions correspond to different ionospheric footprints. We take the next step in 3-D exploration of the ionosphere by presenting the first objective characterization of the primary modes of variability of *E* region, height-dependent conductivities over the entire polar region using spectrally resolved in situ particle measurements from the Special Sensor J (SSJ) instrument on board the F6–F8 and F16–F18 Defense Meteorological Satellite Program (DMSP) satellites. These modes are in the form of empirical orthogonal functions (EOFs) as developed in *McGranaghan et al.*, 2015a [2015a, hereafter M2015] and applied here to altitudes between 100 and 150 km. The first mode captures variability associated with diffuse precipitation [*Newell et al.*, 2009]. The second mode reveals a conductivity response to changes in the interplanetary magnetic field (IMF) B_Z component through the depth of the *E* region. The third mode seems to capture the conductivity effects of Alfvénic Poynting flux-driven broadband electron precipitation in the premidnight and in regions flanking the noon local time (LT) sectors [*Keiling et al.*, 2003; *Chaston et al.*, 2007; *Zhang et al.*, 2014].

The primary modes for height-dependent conductivities are different from the primary height-integrated conductance modes shown in M2015, including a distinct premidnight feature between 110 and 130 km in EOF1, height-dependent premidnight, dawn, and high-latitude dayside LT features in EOF2, and previously absent dayside variability in EOF3. These differences underscore the importance of analyzing the *E* region ionosphere in 3-D.

Our EOFs will support global modeling of 3-D ionospheric electrodynamics. Such specification is important because electric fields and currents are a large source of energy and momentum for the upper atmosphere and is an area where data assimilation has been particularly effective in addressing shortcomings of global models [*Matsuo et al.*, 2005; *Cousins et al.*, 2013a, 2015; *McGranaghan et al.*, 2016]. Quantifying ionospheric conductivity variability supports uncertainty estimation for constraining 3-D data assimilative analyses in the same manner that *McGranaghan et al.* [2016] used two-dimensional (2-D) conductance EOFs to constrain 2-D ionospheric electrodynamics analyses.

2. Data and Methods

We process the same in situ observations from the SSJ instrument on board the F6–F8 and F16–F18 DMSP satellites [*Hardy et al.*, 1984; *Kadinsky-Cade et al.*, 2004] used in M2015 with the GLobal AirglOW (GLOW) model [*Solomon et al.*, 1988; *Solomon and Abreu*, 1989; *Bailey et al.*, 2002] to produce altitude profiles of conductivities at the 1 s cadence of the DMSP electron flux observations without assumption of the electron energy spectra. GLOW yields altitude profiles of ionization and dissociation rates and ion and electron densities, which are used to compute profiles of the Hall and Pedersen conductivities, as described in detail in *McGranaghan et al.* [2015b]. We use the median values over contiguous 60 s intervals, rather than the 60 s running average used in the M2015 height-integrated analysis, because the magnitudes of the height-dependent conductivities are much smaller than the height-integrated values and are more sensitive to outliers. Both techniques yield 60 s resolved values that we call pseudoobservations. We assume hemispheric conjugacy in the pseudoobservations in order to provide sufficient data coverage over the high-latitude regime.

EOF analysis of the pseudoobservations determines the primary modes of variability of the ionospheric Hall and Pedersen conductivities. The EOF analysis follows the methodology described in M2015 that is not repeated here but is applied at 10 km steps between 100 and 150 km. The conductivity variability is a residual field, which encompasses all perturbations from the mean conductivity ($\bar{\boldsymbol{\sigma}}$):

$$\begin{aligned} \boldsymbol{\sigma}'_{100\,\mathrm{km}} &= \boldsymbol{\sigma}_{100\,\mathrm{km}} - \bar{\boldsymbol{\sigma}}_{100\,\mathrm{km}} \\ &\vdots \\ \boldsymbol{\sigma}'_{150\,\mathrm{km}} &= \boldsymbol{\sigma}_{150\,\mathrm{km}} - \bar{\boldsymbol{\sigma}}_{150\,\mathrm{km}} \end{aligned} \tag{1}$$

The $k \times 1$ vector $\boldsymbol{\sigma}'_h$ at altitude h contains the conductivity variability at k locations and a given discrete time, t. A time series of the vector $\boldsymbol{\sigma}'_h$ is decomposed into dominant modes represented by n EOFs and their coefficients as

$$\left[\boldsymbol{\sigma}'_h(t_1), \cdots, \boldsymbol{\sigma}'_h(t_j)\right] = \boldsymbol{\Gamma}_h \mathbf{A}_h + \left[\mathbf{e}'_h(t_1), \cdots, \mathbf{e}'_h(t_j)\right] \tag{2}$$

The $k \times n$ matrix $\boldsymbol{\Gamma}_h$ contains the total of n EOFs evaluated at k grid locations for altitude h, and the $n \times j$ matrix $\mathbf{A}_h$ contains n EOF coefficients at j discrete time periods. The $k \times 1$ vector $\mathbf{e}'_h$ is the residual after subtracting the mean and sum of weighted EOFs from $\boldsymbol{\sigma}_h$. The temporal variation resolution is 1 h, and the spatial resolution of EOFs is 2.5° in latitude and 15° in longitude (yielding a total of $k = 925$ grid points) as in M2015. Here n is chosen to be 3.

To obtain a more robust estimate of the modes of variability, we perform this EOF analysis 25 times using 25 randomly selected subsets of the complete DMSP data set. Each random subset contains 2500 1 h periods (i.e., $j = 2500$), or 20% of the total number, yielding roughly 200,000 data points per subset.

We follow the procedure outlined by *Cousins et al.* [2013b] to obtain a set of average EOFs from 25 independent sets of EOFs. There are three steps to this calculation:

1. Calculate the $k \times k$ covariance matrix by using the EOF coefficients covariance, $\frac{1}{j-1}\mathbf{A}_h\mathbf{A}_h^{\mathrm{T}}$, estimated from j samples for each of these 25 sets as

$$\frac{1}{j-1}\boldsymbol{\Gamma}_h \mathbf{A}_h \mathbf{A}_h^{\mathrm{T}} \boldsymbol{\Gamma}_h^{\mathrm{T}} \tag{3}$$

2. Average the 25 covariance matrices at each altitude.
3. Calculate the first three eigenvalues from the average covariance matrix at each altitude.

To average the 25 covariance matrices at each altitude, we calculate the 25 normalized correlation matrices and average them element by element. We then specify the diagonal elements (the variances) as the medians

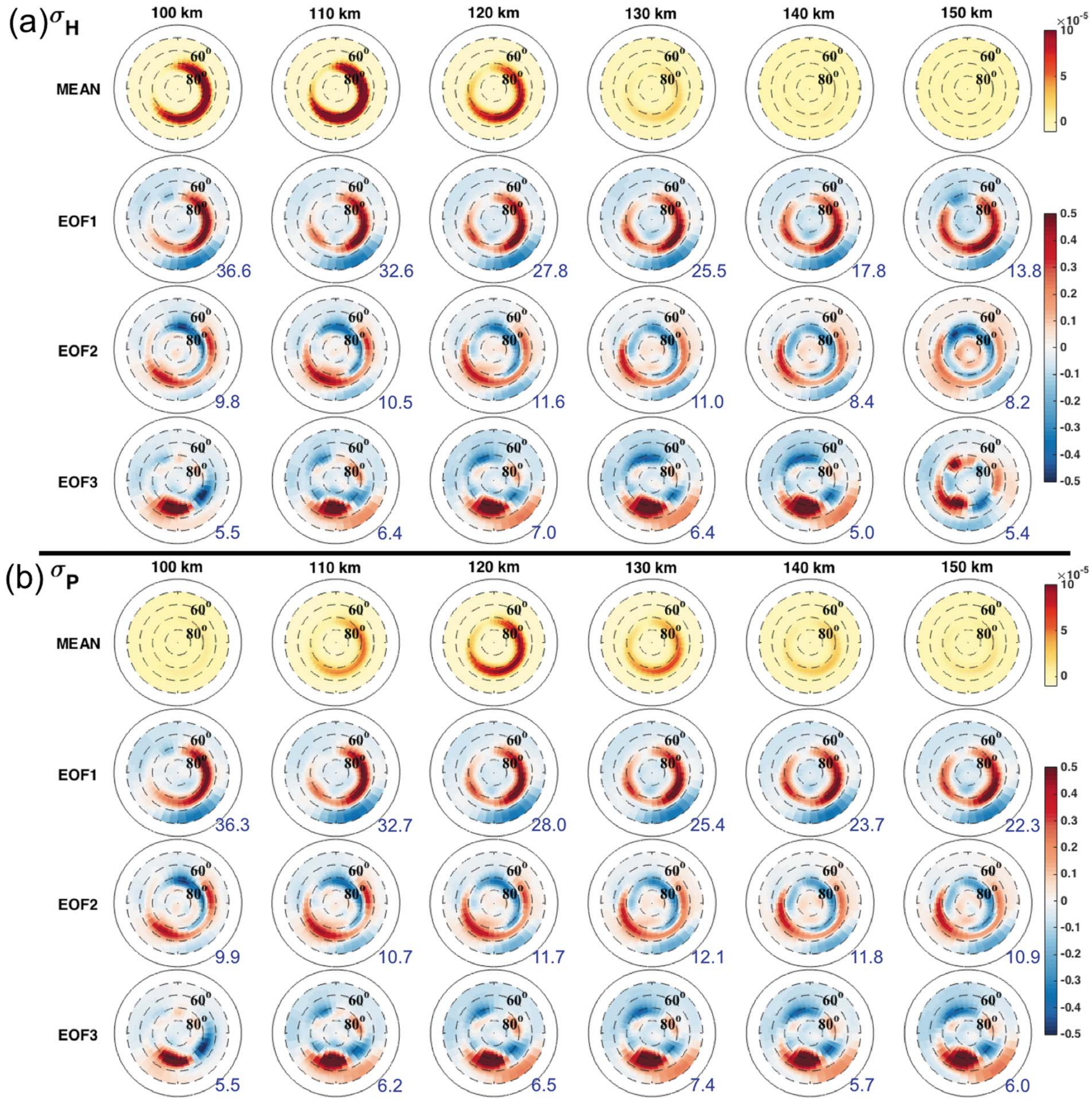

Figure 1. The mean and first three modes of variability (average EOFs) in the *E* region ionosphere for (a) Hall conductivities (σ_H) and (b) Pedersen conductivities (σ_P). Mean patterns are along the top of Figures 1a and 1b with a linear color scale (yellow to red), and EOFs are beneath the mean patterns with a diverging color scheme (blue to red) and scaled to a −0.5 to 0.5 range. The altitude increases from left to right. Each polar plot is oriented with the Sun off to the top of the figure, dawn to the right, and dusk to the left and displays the distributions in AACGM coordinates. The percentage of the overall variability captured by each EOF is given in blue at bottom right.

of each diagonal element across all 25 samples. Finally, the average covariance matrix is reconstructed from the average correlation matrices and median values of the variances. We then compute the first three EOFs from the eigenvalue decomposition of the average covariance matrix. The result is a set of three EOFs for each altitude. These average EOFs are presented in this work.

3. Results: Three-Dimensional High-Latitude *E* Region Conductivity

Figures 1a and 1b show the mean and first three EOFs for the Hall and Pedersen conductivities, HEOF and PEOF, respectively. The mean patterns are in the top row. The EOFs are beneath the mean patterns. Each polar plot is oriented with noon at the top. The distributions are shown in altitude adjusted corrected geomagnetic (AACGM) coordinates.

The mean Hall and Pedersen conductivities show a large-scale, crescent-shaped conductivity feature, consistent with the atmospheric imprint of diffuse auroral precipitation from the magnetosphere [*Winningham et al.*, 1975; *McGranaghan et al.*, 2015a, and references therein]. Altitudinal variations of the patterns peak at 110 km for the Hall conductivity and at 120 km for Pedersen conductivity. This structuring reflects the relative motions of ions and electrons in the upper atmosphere. At lower altitudes more frequent ion-neutral collisions retard the motion of the ions and produce a current carried by the more mobile electrons drifting in the $E \times B$ direction (Hall current). At higher altitudes where the electrons are strongly magnetized but significant collisions cause the drifting ions to attain a component of motion in the electric field direction, the current is carried by the ions in the direction of E (Pedersen current). Pedersen conductivity becomes the dominant term between 120 and 130 km [*Richmond and Thayer*, 2000]. Above 150 km both conductivities typically decrease exponentially with altitude. The mean Hall and Pedersen fields reflect the ion and electron mobilities, with the Hall and Pedersen conductivities maximizing between 100 and 120 km and 110 and 130 km, respectively. The auroral enhancement of the mean Hall conductivity exhibits a clockwise rotation in LT with increasing altitude.

After removing the mean components, different for each altitude, the first EOFs represent the primary mode of variability in the residual. Variability about the mean patterns (EOF1, second row) is fairly uniform with height, showing a general tendency for the peak variability to migrate from the postdawn sector to the predawn sector with increasing altitude. Between 110 and 130 km a distinct premidnight intensity region appears.

The percentage of the overall variability captured by each EOF is shown in bottom right of each plot. EOF1 captures 30–40% of the variability at lower altitudes, and generally 20–30% above 120 km altitude. Supporting information Figure S1 shows the complete distribution of the overall variability among the EOFs. The EOF1 patterns are consistent with geomagnetic-activity-driven variations of the diffuse aurora.

The Hall and Pedersen conductivity EOF2 fields show similar variations with altitude between 110 and 140 km, consistent with the ionospheric conductivity response to enhanced magnetospheric convection [*Kamide et al.*, 1996; *Kamide and Kokubun*, 1996; *McGranaghan et al.*, 2015a]. The structured features in EOF2 are poleward and equatorward of the peaks in the EOF1 patterns. These features are the hallmarks of expansion and contraction of the auroral oval as geomagnetic activity waxes and wanes. We discuss this further in section 4. EOF2 represents 10% of the overall variability at all altitudes.

The EOF3 Hall and Pedersen conductivity fields are characterized by smaller-scale features. EOF3 represents 5–8% of the overall variability throughout the E region altitudes. Two prominent responses appear, each consistent with the positions of ionospheric broadband precipitation [*Newell et al.*, 2009]. The first in the 21–01 LT sector spans a wide magnetic latitude (MLAT) band. In M2015 this feature was associated with substorm activity. The extension of this response to earlier LTs in a narrow latitudinal region between 60 and 70° is apparent in *Newell et al.* [2009]. The second response is a pair of features at MLAT >70° surrounding the noon LT meridian. The feature in the postnoon region has increasing intensity up to an altitude of 140 km.

To explore the possible geophysical drivers of the modes of variability represented by the EOFs in Figure 1, we correlate the amplitude of each EOF at a given time with the corresponding hourly time series of various solar wind parameters and geophysical indices. These include the IMF B_Z component, the solar wind pressure (psw), geomagnetic indices (auroral electrojet (*AE*), planetary (*Kp*), polar cap (*PC*), and disturbance storm time (*Dst*)), and specialized coupling functions (interplanetary electric field, E_Y, Borovsky coupling function (CF) [*Borovsky*, 2013], and Newell CF [*Newell et al.*, 2007]). These CFs quantify the solar wind-magnetospheric connection and are, therefore, germane to our discussion of solar wind-magnetosphere-ionosphere (SWMI) coupling. For each of the 25 subsets used to construct the average EOFs in Figure 1, we calculate the correlation coefficient between each parameter/index and each EOF amplitude. This gives 25 correlation coefficients for each parameter/index-EOF combination (for instance, 25 correlation coefficients between IMF B_Z and HEOF1). We then calculate the median of these 25 correlations and display that value in Figure 2. This process is carried out separately for each altitude level. Figures 2a–2c show these median correlations for HEOFs 1–3, respectively, and Figures 2d–2f show the correlations for PEOFs 1–3. Each altitude is represented by a different color.

Consistent with the correlations of the ionospheric conductance EOF1 amplitudes in M2015, Figures 2a and 2d demonstrate that the amplitudes of the first EOFs correlate with geomagnetic activity (B_Z, the geomagnetic indices, and CFs). At lower altitudes HEOF1 is more strongly correlated with the parameters tested. The PEOF1 correlations are more uniform with altitude. HEOF2 correlations show the largest correlations at 120–140 km. There is a similar separation of PEOF2 correlations, with the largest correlations between 120 and 150 km. The

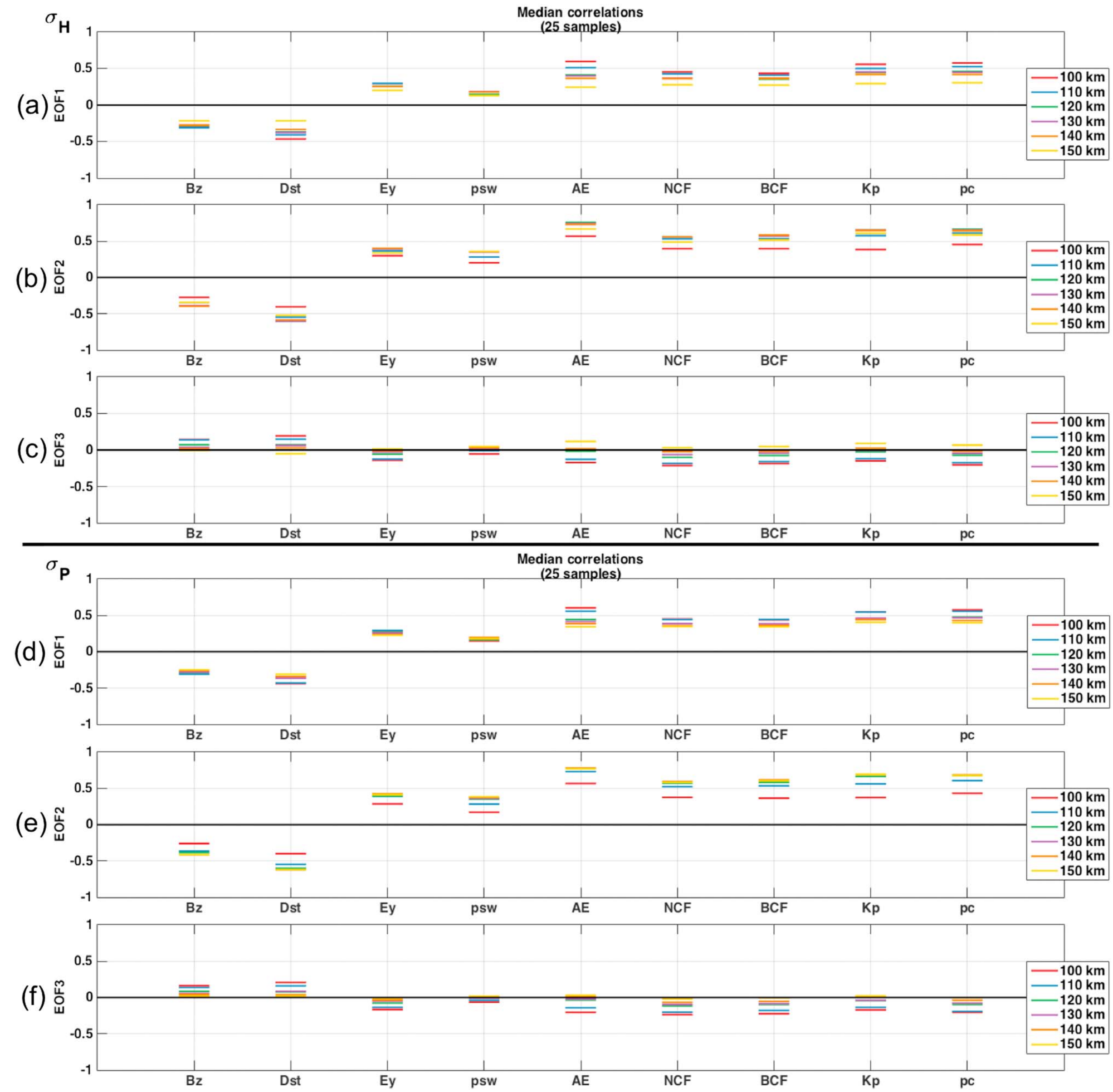

Figure 2. Correlations between temporal EOF amplitudes and hourly averaged solar wind parameters and geomagnetic indices described in section 3. (a–c) HEOF1-3 correlations. (d–f) PEOF1-3 correlations. Altitudes are shown by different colors.

correlations are smallest at 100 km for both patterns. The correlations of HEOF3 and PEOF3 are reduced with respect to EOF1 and EOF2 but are largest at 100 km, and small at higher altitudes.

In general, the spread of correlation coefficients for each parameter/index-EOF across the 25 samples was small (not shown). The standard deviations were typically ~0.02–0.05 for all combinations of parameter/index-EOF below 140 km. At 140–150 km, the standard deviations of correlation coefficients for the index and CF correlations increase to ~0.1 for EOF2 and ~0.2 for EOF3.

4. Discussion

Two findings revealed by the height-dependent analysis are of note: the relationship between EOF2 and IMF B_Z and the EOF3 association with Poynting flux. Figure 3 sketches the SWMI system behavior that we believe

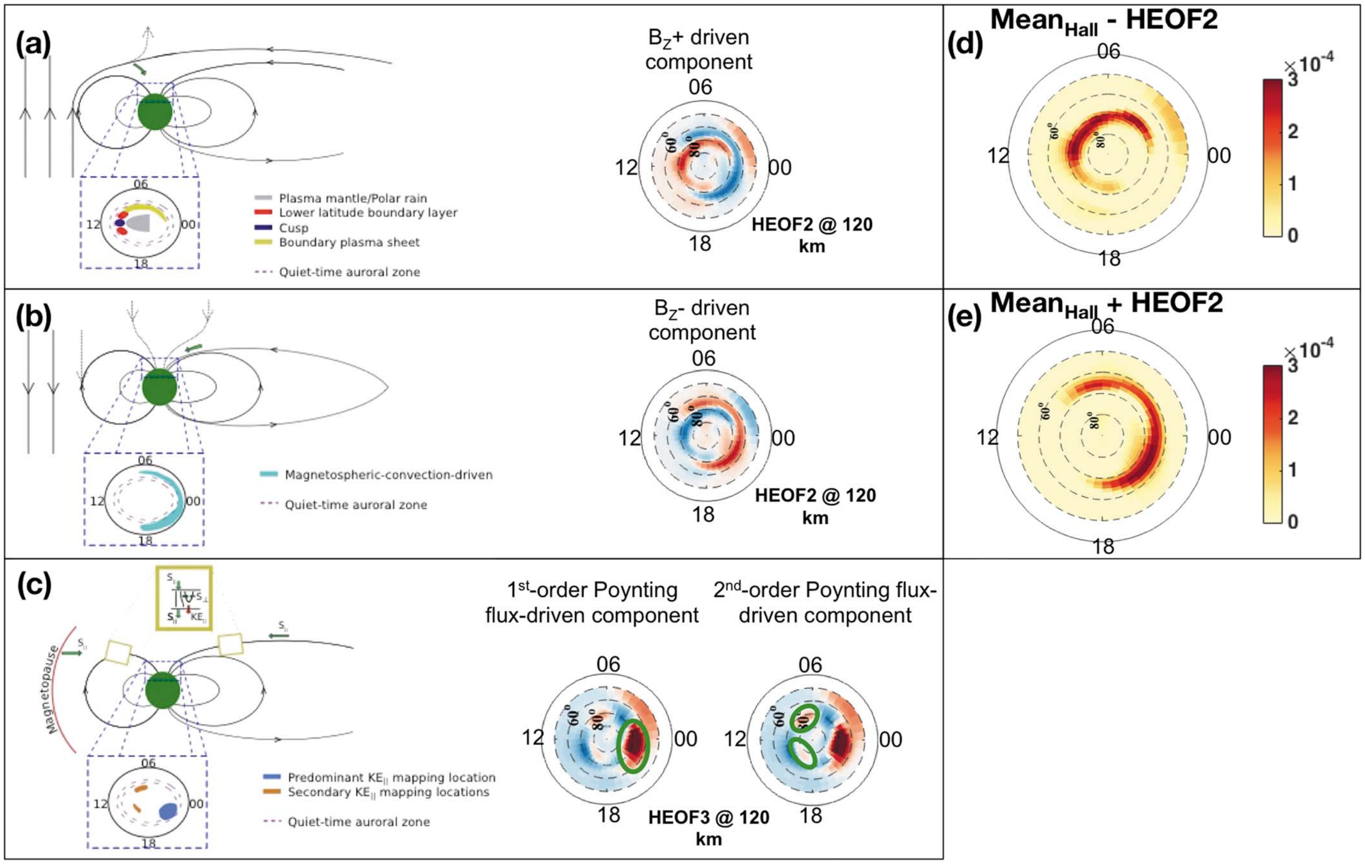

Figure 3. Representation of the SWMI system during different conditions that each relate to unique modes of conductivity variability. Each SWMI schematic is at the left with the accompanying mode of variability to its right. The HEOF patterns at 120 km are used for the illustrations. The Sun is to the left. (a) IMF $+B_Z$ supports poleward-of-the-cusp dayside reconnection that enhances electron precipitation into the high-latitude dayside ionosphere. (b) IMF $-B_Z$ supports strong reconnection that enhances magnetospheric convection. The resultant electron precipitation maps to a latitudinally expanded, nightside ionospheric region. The variations associated with $+B_Z$ and $-B_Z$ IMF are oppositely signed and occur simultaneously as illustrated by oppositely signed HEOF2 patterns. (c) Field-aligned Alfvénic Poynting flux ($S_{||}$) supports Alfvénic waves propagating from the magnetopause and magnetotail to acceleration regions (shown in the yellow boxes), where the field-aligned Alfvénic waves either map through to the ionosphere or converge ($S_{\perp}$) and drive kinetic energy divergence ($KE_{||}$) and broadband accelerated electrons into the ionosphere. The predominant mapping locations in the ionosphere are premidnight and two locations flanking noon LT. Mean Hall conductivity distributions augmented by HEOF2: (d) $\alpha^{(2)}$*HEOF2 subtracted from the mean pattern ($+B_Z$ conditions) and (e) $\alpha^{(2)}$*HEOF2 added to the mean pattern ($-B_Z$ conditions). The $\alpha^{(2)}$ amplitude chosen for this display is from 0200 to 0300 UT 24 September 2010 ($B_Z \sim -4.0$ nT).

leads to the EOF2 (Figures 3a and 3b) and EOF3 (Figure 3c) conductivity variabilities. We take the HEOF patterns at 120 km (provided to the right in each panel of Figures 3a–3c) to be representative. Relationships between the SWMI behavior, particle precipitation mapping locations, and ionospheric conductivities are discussed below.

4.1. Relationship Between EOF2 and IMF B_Z

IMF B_Z affects the conductivity variability in each of the first three modes. However, EOF2 characterizes an important relationship between IMF B_Z and the variability in the structured aurora associated with accelerated precipitating electrons, which we discuss here. These EOF2 patterns identify two clear, spatially delineated conductivity responses, distinguished by the direction of B_Z: (1) under southward directed B_Z ($-B_Z$), conductivities are enhanced in the latitudinally expanded auroral oval, consistent with the expanding/contracting polar cap paradigm [*Cowley and Lockwood*, 1992; *Milan et al.*, 2012]; and (2) under northward directed B_Z ($+B_Z$), conductivities are enhanced at MLATs >70° and dayside LTs, consistent with precipitation from boundary plasma regions (BPRs) [*Vasyliunas*, 1979; *Rich et al.*, 1990; *Newell and Meng*, 1992; *Newell et al.*, 2009]. The term BPR refers to the ionospheric regions that map to the magnetospheric boundary layers as discussed in *Vasyliunas* [1979] and *Rich et al.* [1990], including the boundary plasma sheet, low-latitude boundary layer, mantle, and cusp/cleft (see Figure 1 in *Vasyliunas* [1979], provided as supporting information).

EOF2 is anticorrelated with B_Z (Figures 2b and 2e), indicating that the conductivity variability increases with the magnitude of southward IMF B_Z, the level of solar wind-magnetospheric coupling, and enhanced magnetospheric convection and Region 1/2 field-aligned currents (FACs) [*Iijima and Potemra*, 1978; *Cowley and Lockwood*, 1992; *Kamide et al.*, 1996, *Milan et al.*, 2007, 2012; *Coxon et al.*, 2015]. The EOF2 patterns also correlate strongly with the Borovsky and Newell CFs.

EOF2 suggests a mode of variability with high- and low-latitude components that vary in tandem, depending on the direction of B_Z. To demonstrate the relationship between $-B_Z$ and positive EOF2 amplitude (and, likewise, between $+B_Z$ and negative amplitude), Figures 3d and 3e show the mean Hall conductivity distributions augmented by the HEOF2 patterns during a period of $-B_Z$ (24 September 2010 0200–0300 UT, $B_Z = -4.0$). During this period, the sign of HEOF2 is positive, indicating that the HEOF2 pattern in Figure 1 should be added to the mean pattern. Note that the contribution of EOF1 and associated influence of the diffuse aurora are excluded in order to emphasize the structured, spatially delineated effects captured by EOF2. The conductivity is shown in Figure 3e and corresponds to the situation depicted in Figure 3b. The mean conductivity is clearly strengthened and dominated by the latitudinally expanded auroral region conductivity. To examine the conductivity variability associated with $+B_Z$, we instead subtract the EOF2 contribution from the mean. This situation is shown in Figure 3d and corresponds to Figure 3a. The latitudinally expanded conductivity is replaced by enhancement in the dayside high-latitude features that become prominent under $+B_Z$.

We assert that the two components of EOF2 can be associated with the magnetospheric source location of the precipitating electrons (excluding the diffuse precipitation component, which was accounted for in EOF1). Under $-B_Z$ the precipitation is dominated by accelerated electrons, both monoenergetic and broadband, mapping to the central plasma sheet (CPS) [*Newell et al.*, 2009]. The CPS precipitation correlates with the large-scale Region 1/2 FACs and maps to the expanded auroral oval [*Iijima and Potemra*, 1978; *Kamide et al.*, 1996]. As the IMF turns northward the precipitation primarily originates in the BPR, which maps to the high latitudes and dayside ionosphere along a configuration of FACs consisting of the Northward B_Z (NBZ) and high-latitude Region 1 systems [*Iijima and Potemra*, 1976a, 1976b; *Vasyliunas*, 1979; *Rich et al.*, 1990]. Figure 3a illustrates the $+B_Z$ SWMI behavior consistent with high-latitude magnetic merging (see also Figure 19 in *Maezawa* [1976], provided as supporting information) and the high-latitude dayside mapping location of the BPRs. The HEOF2 pattern at 120 km reflects this behavior. *Rich et al.* [1990] reported that during intervals of well-defined $-B_Z$ and $+B_Z$ "[the shrinkage] of the latitudinal width of the CPS was coincident with the disappearing of the auroral zone Region 1/2 currents. In addition, the expansion of the BPR to higher latitudes occurred simultaneously with the appearing of the NBZ current system." These aspects of magnetosphere-ionosphere (MI) coupling due to IMF B_Z are in agreement with our results for the ionospheric conductivity variabilities.

4.2. Relationship Between EOF3 and Alfvén Poynting Flux

Here we relate broadband precipitation to conductivity variability represented by EOF3. The predominant driver of broadband precipitation is the convergence of Alfvénic Poynting flux ($S_\perp$) in the auroral acceleration region (AAR, located at altitudes between ~0.2 and 2 Earth radii [*Forsyth et al.*, 2012]) causing a divergence of particle kinetic energy flux ($KE_{||}$) over a broad range of energies into the ionosphere [*Lotko*, 1986; *Thayer and Semeter*, 2004; *Newell et al.*, 2009]. A more direct connection was established between broadband electron precipitation and $S_\perp$ on the basis of in situ satellite observations above and below the AAR, showing that broadband precipitation is largely driven by dispersive Alfvén waves [*Wygant and Keiling*, 2000; *Andersson et al.*, 2002; *Keiling et al.*, 2003; *Chaston et al.*, 2007]. Although the connection between $S_\perp$ and ionospheric conductivity variability remains an open question in MI studies, our EOF3 results suggest that $S_\perp$ plays an important role in modifying ionospheric conductivities via particle precipitation.

The premidnight location of EOF3 is consistent with the primary ionospheric mapping location of broadband electrons. *Chaston et al.* [2007] and *Zhang et al.* [2014] showed that Alfvénic Poynting flux convergence in the premidnight regime is several times more energetic than on the dayside and that this pattern also appears in the energetic electron fluxes. The premidnight feature is prominent in our EOF3 patterns as well.

The dayside (secondary) broadband enhancement [*Chaston et al.*, 2005], captured as prenoon and postnoon LT features in the EOF3 patterns, is related to less intense conductivity variability. *Newell et al.* [2009] found that the broadband precipitation was extremely common in the prenoon LT location and is accordingly more pronounced than the postnoon dayside feature in our results. The dayside regions of enhanced conductivities presumed to be due to broadband precipitation are highly variable with altitude. These locations of broadband precipitation are likely more directly controlled by the IMF B_Y direction, to which our results are not sensitive because we assume hemispheric conjugacy. This may contribute to the variability of the locations and intensities of these regions in our EOF3 patterns. Nevertheless, we argue that these regions indicate that broadband precipitation effectively modifies ionospheric conductivity in the dayside, as well as the nightside, high-latitude regions.

Figure 3c illustrates the SWMI system and $S_\perp$ progression leading to variability of the ionospheric conductivities. The green rings on the inset HEOF3 patterns identify the regions we interpret as the ionospheric locations of broadband electron precipitation. Simultaneous observations above and below the AAR will provide data to further investigate the $S_\perp$-ionospheric conductivity connection and is specified as important future work.

We have limited our discussion of EOF3 to the features that we assert are driven by $S_\perp$. Interpretation of additional features, such as that in the postmidnight LT sector with opposite sense to the premidnight feature, is difficult given the comparatively small contribution of this mode to the total variance (5–8%).

4.3. Comparison of EOF Results and Precipitation Characteristics

While the EOFs derived from millions of DMSP spectra do not represent direct relationship between conductivity variability and precipitating particles, we may examine statistical precipitation patterns to evaluate the connections between EOF2 with monoenergetic precipitation and EOF3 with broadband precipitation using the criteria of several studies [*Newell et al.*, 1996, 2007, 2009, hereafter referred to as N1996, N2007, and N2009]. We compare the N2009 patterns created from DMSP data acquired in 1988–1998 with our EOF patterns for the month of January 2010, which reveals similar information to a longer-period analysis from which the EOFs are derived. Figure 4 shows the results.

Figure 4a shows the accelerated precipitation spectra binned into the EOF analysis grid. Figure 4b reproduces the HEOF2 and HEOF3 patterns at 120 km, taken to be representative of the general patterns for comparison. Figures 4c and 4d, respectively, reproduce the accelerated precipitation spectra number and energy fluxes from N2009. All plots in a given column are related (e.g., Figures 4a1, 4b1, 4c1, and 4d1 are related).

Regarding the relationship between EOF2 and monoenergetic precipitation (Figures 4a1, 4b1, 4c1, and 4d1, and 4a2, 4b2, 4c2, and 4d2, respectively), steady state dayside magnetic reconnection primarily produces monoenergetic electron precipitation into the most poleward and equatorward ionospheric auroral boundaries (N1996), which suggests that EOF2 is related to conductivity variability driven in large part by monoenergetic precipitation. Figures 4a1, 4b1, 4c1, and 4d1, and 4a2, 4b2, 4c2, and 4d2 compare our results with the N2009 number and energy fluxes of monoenergetic electron precipitation. Figures 4a1 and 4a2 show the locations of ~130,000 monoenergetic electron precipitation spectra identified using the N2009 criteria, separated according to $+B_Z$ (Figure 4a1, 60,013 spectra) and $-B_Z$ (Figure 4a2, 70,270 spectra). These figures show that occurrence of monoenergetic precipitation is common in the dayside high-latitude regions flanking noon LT for $+B_Z$, with occurrences increasing in the dusk and nightside LT sectors for $-B_Z$. Figures 4b1 and 4b2 show the HEOF2 patterns at 120 km that correspond to $+B_Z$ and $-B_Z$, respectively. Figures 4c1 and 4c2 reproduce the N2009 monoenergetic number flux during low- and high-solar wind driving (their Figure 7), respectively. There is a close correspondence between the occurrence of monoenergetic precipitation during $+B_Z$ and low-solar wind driving and during $-B_Z$ and high-solar wind driving. Figures 4d1 and 4d2 show the same thing as Figures 4c1 and 4c2 except for the monoenergetic precipitation energy flux. The conductivity variability is dependent on the particle precipitation, here represented by the number and energy flux of precipitating electrons, and the state of the upper atmosphere. During low-solar wind driving/$+B_Z$ the EOF2 pattern in Figure 4b1 captures the high dayside number flux convolved with the relatively low-level energy flux that extends through the morning and dayside LTs between 75 and 80°. Under high-solar wind driving/$-B_Z$ the EOF2 pattern in Figure 4b2 captures conductivity variability that reflects the latitudinally expanded regions of enhanced number and energy flux at LTs extending from dusk through midnight to morning.

There are some differences, including (1) representation of our EOFs by polar cap spherical harmonics basis functions versus the straightforward binning used to create the Newell maps (2) different analysis time periods (our EOFs: 1987 and 2010 versus Newell's maps: 1988–1998), and (3) different binning (the level of solar wind driving used to bin results in N2009, determined by the N2007 NCF, is not identical to our separation by B_Z direction). Additionally, despite the influence of monoenergetic precipitation in the conductivity variability in EOF2, this variability also likely depends on other compounding factors.

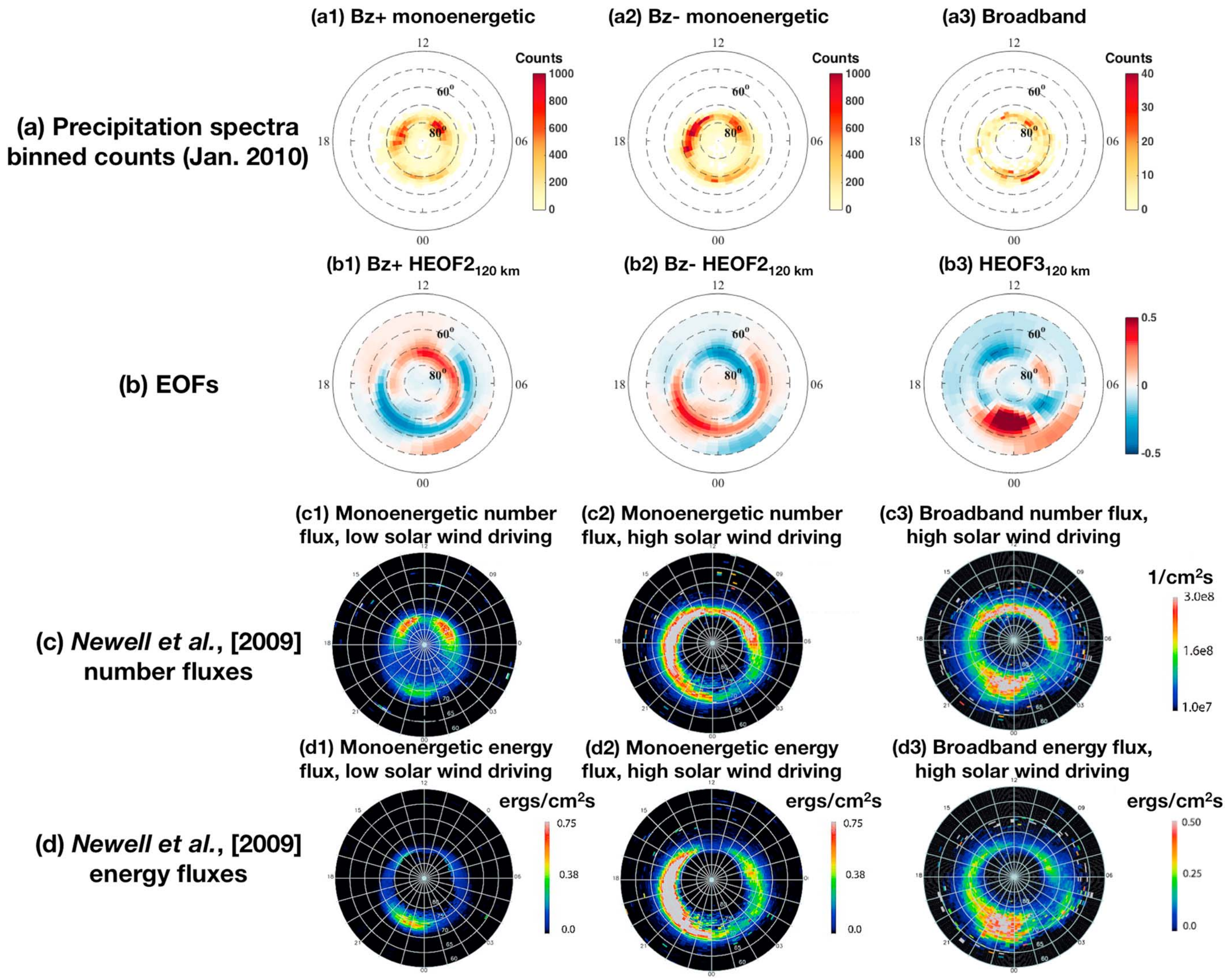

Figure 4. Particle precipitation characteristics for January 2010. (a) The occurrences (or counts) of precipitation spectra binned into the EOF grid for monoenergetic precipitation during (a1) $+B_Z$ and during (a2) $-B_Z$ and precipitation spectra for (a3) broadband precipitation. (b) EOFs, using the HEOF patterns at 120 km as representative: (b1) HEOF2 during B_Z+ conditions, (b2) HEOF2 during B_Z- conditions, and (b3) HEOF3. (c) Precipitation number flux averaged over 1988–1998, reproduced from N2009, for monoenergetic precipitation: (c1) under low-solar wind driving (based on the N2007 NCF), (c2) under high-solar wind driving, and (c3) broadband precipitation under high-solar-wind driving. (d) same as Figure 4c except for energy fluxes.

Figures 4a3, 4b3, 4c3, and 4d3 show the broadband precipitation characteristics for January 2010, HEOF3 pattern at 120 km, and the N2009 broadband precipitation statistical distributions. Figure 4a3 shows the locations of the 1383 broadband precipitation spectra identified using the N2009 criteria binned into the EOF analysis grid. In these figures the broadband precipitation occurs frequently in the dayside high-latitude regime, and there is also frequent broadband precipitation into the nightside LT sector consistent with the premidnight conductivity variability.

Figures 4c3 and 4d3 reproduce the high-solar-wind-driven (specified by the N2007 NCF) broadband precipitation number and energy fluxes, respectively, from N2009. The energy flux corresponds closely with the HEOF3 pattern in Figure 4b3, with the most intense precipitation and largest conductivity variability in the premidnight LT sector. The dayside locations have less energetic broadband precipitation and correspondingly reduced conductivity variability. Thus, we call these second-order broadband features. Figure 4c3 shows that the broadband precipitation number flux is more evenly divided between the dayside and premidnight features, and the number flux peaks in the prenoon location, where broadband accelerated electron events are extremely common. Figure 4a3 also shows a large number of precipitation events in this region in the January 2010 data.

The nonlinearities in the MI system preclude a one-to-one connection between any single conductivity EOF and any single type of precipitation, which is one reason for differences between our EOFs and the statistical patterns of precipitation. Nonetheless, these comparisons provide further evidence of the close EOF2-B_Z/EOF3-$S_\perp$ relationships. Future work will produce EOFs directly from DMSP energy flux measurements to better characterize the precipitation variability and understand underlying physical mechanisms.

5. Conclusions

We have conducted the first EOF analysis of global height-dependent ionospheric conductivities based on in situ energetic electron precipitation measurements from DMSP spacecraft. No assumption regarding the electron energy spectra was made. Our 3-D EOFs reveal two previously unidentified characteristics of ionospheric conductivity variability: (1) a clear, spatially delineated relationship between conductivity variability and the direction of IMF B_Z in EOF2 and (2) the likely influence of Alfvénic Poynting flux-driven broadband electron precipitation on the conductivity variability in EOF3, separated into a first-order effect in the premidnight LT sector and second-order effects flanking the noon LT sector. These relationships may be exploited in future ionospheric conductivity specification and forecasting efforts.

The EOFs exhibit distinct altitude-dependent behavior, and differences from EOFs derived in the same manner for height-integrated conductances in *McGranaghan et al.* [2015a]. These differences suggest that height-integrated and height-dependent characterizations of the ionosphere are distinctly different and underscore the importance of analyzing the *E* region ionosphere in 3-D.

These EOFs can be used to create a realistic conductivity model error covariance for application to ionospheric data assimilative techniques in the same manner that height-integrated conductivity EOFs were used to improve specification of 2-D ionospheric electrodynamics in *McGranaghan et al.* [2016]. Therefore, these results enable 3-D specification of the ionospheric electrodynamics and will enhance understanding of auroral particle precipitation, ionospheric electric fields, and field-aligned currents and the complex relationships between them.

Acknowledgments
R.M.G. was partially supported by NSF Fellowship award DGE 1144083 and NASA grant NNX13AD64G. D.J.K. was partially supported by NSF grant AGS 1144154 and NASA grant NNX13AG07G. T.M. was supported by NSF grant PLR-1443703 and NASA grant NNX14AI17G. T.M. is grateful for Olaf Amm who originally provided inspiration for 3-D high-latitude ionospheric electrodynamics. We thank Art Richmond for useful discussions. NCAR is supported by the NSF. We gratefully acknowledge the NASA Space Physics Data Facility; the World Data Center, Kyoto; and the National Geophysical Data Center for providing the high-resolution OMNI data, the *AE* and *SYM-H* index data, and the *Kp* index data, respectively. We thank Rob Redmon and the National Center for Environmental Information (NCEI) for providing the DMSP particle data, which were obtained from NASA CDAWeb (http://cdaweb.gsfc.nasa.gov/).

References

Amm, O., A. Aruliah, S. C. Buchert, R. Fujii, J. W. Gjerloev, A. Ieda, T. Matsuo, C. Stolle, H. Vanhamäki, and A. Yoshikawa (2008), Towards understanding the electrodynamics of the 3-dimensional high-latitude ionosphere: Present and future, *Ann. Geophys.*, *26*(12), 3913–3932, doi:10.5194/angeo-26-3913-2008.

Andersson, L., N. Ivchenko, J. Clemmons, A. A. Namgaladze, B. Gustavsson, J.-E. Wahlund, L. Eliasson, and R. Y. Yurik (2002), Electron signatures and Alfvén waves, *J. Geophys. Res.*, *107*(A9), 1244, doi:10.1029/2001JA900096.

Bailey, S. M., C. A. Barth, and S. C. Solomon (2002), A model of nitric oxide in the lower thermosphere, *J. Geophys. Res.*, *107*(A8), 1205, doi:10.1029/2001JA000258.

Borovsky, J. E. (2013), Physical improvements to the solar wind reconnection control function for the Earth's magnetosphere, *J. Geophys. Res. Space Physics*, *118*, 2113–2121, doi:10.1002/jgra.50110.

Chaston, C. C., et al. (2005), Energy deposition by Alfvén waves into the dayside auroral oval: Cluster and FAST observations, *J. Geophys. Res.*, *110*, A02211, doi:10.1029/2004JA010483.

Chaston, C. C., C. W. Carlson, J. P. McFadden, R. E. Ergun, and R. J. Strangeway (2007), How important are dispersive Alfvén waves for auroral particle acceleration?, *Geophys. Res. Lett.*, *34*, L07101, doi:10.1029/2006GL029144.

Cousins, E. D. P., T. Matsuo, and A. D. Richmond (2013a), SuperDARN assimilative mapping, *J. Geophys. Res. Space Physics*, *118*, 7954–7962, doi:10.1002/2013JA019321.

Cousins, E. D. P., T. Matsuo, and A. D. Richmond (2013b), Mesoscale and large-scale variability in high-latitude ionospheric convection: Dominant modes and spatial/temporal coherence, *J. Geophys. Res. Space Physics*, *118*, 7895–7904, doi:10.1002/2013JA019319.

Cousins, E. D. P., T. Matsuo, and A. D. Richmond (2015), Mapping high-latitude ionospheric electrodynamics with SuperDARN and AMPERE, *J. Geophys. Res. Space Physics*, *120*, 5854–5870, doi:10.1002/2014JA020463.

Cowley, S. W. H., and M. Lockwood (1992), Excitation and decay of solar wind-driven flows in the magnetosphere-ionosphere system, *Ann. Geophys.*, *10*, 103–115.

Coxon, J. C., S. E. Milan, L. B. N. Clausen, B. J. Anderson, and H. Korth (2015), The magnitudes of the regions 1 and 2 Birkeland currents observed by AMPERE and their role in solar wind-magnetosphere-ionosphere coupling, *J. Geophys. Res. Space Physics*, *119*, 9804–9815, doi:10.1002/2014JA020138.

Forsyth, C., et al. (2012), Temporal evolution and electric potential structure of the auroral acceleration region from multispacecraft measurements, *J. Geophys. Res.*, *117*, A12203, doi:10.1029/2012JA017655.

Hardy, D. A., L. K. Schmidt, M. S. Gussenhoven, F. J. Marshall, H. C. Yeh, T. L. Shumaker, A. Huber, and J. Pantazis (1984), Precipitating electron and ion detectors (SSJ/4) for the Block 5D/flights 6-10 DMSP satellites: Calibration and data presentation, Tech. Rep. ADA157080, Air Force Geophys. Lab., United States Air Force, Hanscom Air Force Base, Mass.

Iijima, T., and T. A. Potemra (1976a), The amplitude distribution of field-aligned currents at northern high latitudes observed by Triad, *J. Geophys. Res.*, *81*(13), 2165–2174, doi:10.1029/JA081i013p02165.

Iijima, T., and T. A. Potemra (1976b), Field-aligned currents in the dayside cusp observed by Triad, *J. Geophys. Res.*, *81*(34), 5971–5979, doi:10.1029/JA081i034p05971.

Iijima, T., and T. A. Potemra (1978), Large-scale characteristics of field-aligned currents associated with substorms, *J. Geophys. Res.*, *83*(A2), 599–615, doi:10.1029/JA083iA02p00599.

Kadinsky-Cade, K., E. G. Holeman, J. McGarrity, F. J. Rich, W. F. Denig, W. J. Burke, and D. A. Hardy (2004), First results from the SSJ5 precipitating particle sensor on DMSP F16: Simultaneous observation of keV and MeV particles during the 2003 Halloween storms, *Eos Trans. AGU*, *85*(17), Jt. Assem. Suppl., Abstract SH53A–03.

Kamide, Y., and S. Kokubun (1996), Two-component auroral electrojet: Importance for substorm studies, *J. Geophys. Res.*, *101*(A6), 13,027–13,046, doi:10.1029/96JA00142.

Kamide, Y., W. Sun, and S.-I. Akasofu (1996), The average ionospheric electrodynamics for the different substorm phases, *J. Geophys. Res.*, *101*(A1), 99–109, doi:10.1029/95JA02990.

Keiling, A., J. R. Wygant, C. A. Cattell, F. S. Mozer, and C. T. Russell (2003), The global morphology of wave Poynting flux: Powering the aurora, *Science*, *299*(5605), 383–386, doi:10.1126/science.1080073.

Lilensten, J., P. L. Blelly, W. Kofman, and D. Alcaydé (1997), Auroral ionospheric conductivities: A comparison between experiment and modeling, and theoretical $F_{10.7}$-dependent model for EISCAT and ESR, *Ann. Geophys.*, *14*(12), 1297–1304, doi:10.1007/s00585-996-1297-7.

Lotko, W. (1986), Diffusive acceleration of auroral primaries, *J. Geophys. Res.*, *91*(A1), 191–203, doi:10.1029/JA091iA01p00191.

Lynch, K. A., and D. L. Hampton (2015), MICA sounding rocket observations of conductivity-gradient-generated auroral ionospheric responses: Small-scale structure with large-scale drivers, *J. Geophys. Res. Space Physics*, *120*, 9661–9682, doi:10.1002/2014JA020860.

Maezawa, K. (1976), Magnetospheric convection induced by the positive and negative Z components of the interplanetary magnetic field: Quantitative analysis using polar cap magnetic records, *J. Geophys. Res.*, *81*(13), 2289–2303, doi:10.1029/JA081i013p02289.

Matsuo, T., A. D. Richmond, and G. Lu (2005), Optimal interpolation analysis of high-latitude ionospheric electrodynamics using empirical orthogonal functions: Estimation of dominant modes of variability and temporal scales of large-scale electric fields, *J. Geophys. Res.*, *110*, A06301, doi:10.1029/2004JA010531.

McGranaghan, R., D. J. Knipp, T. Matsuo, H. Godinez, R. J. Redmon, S. C. Solomon, and S. K. Morley (2015a), Modes of high-latitude auroral conductance variability derived from DMSP energetic electron precipitation observations: Empirical orthogonal function analysis, *J. Geophys. Res. Space Physics*, *120*, 11,013–11,031, doi:10.1002/2015JA021828.

McGranaghan, R., D. J. Knipp, S. C. Solomon, and X. Fang (2015b), A fast, parameterized model of upper atmospheric ionization rates, chemistry, and conductivity, *J. Geophys. Res. Space Physics*, *120*, 4936–4949, doi:10.1002/2015JA021146.

McGranaghan, R., D. J. Knipp, T. Matsuo, and E. Cousins (2016), Optimal interpolation analysis of high-latitude ionospheric Hall and Pedersen conductivities: Application to assimilative ionospheric electrodynamics reconstruction, *J. Geophys. Res. Space Physics*, *121*, 4898–4923, doi:10.1002/2016JA022486.

Milan, S. E., G. Provan, and B. Hubert (2007), Magnetic flux transport in the Dungey cycle: A survey of dayside and nightside reconnection rates, *J. Geophys. Res.*, *112*, A01209, doi:10.1029/2006JA011642.

Milan, S. E., J. S. Gosling, and B. Hubert (2012), Relationship between interplanetary parameters and the magnetopause reconnection rate quantified from observations of the expanding polar cap, *J. Geophys. Res.*, *117*, A03226, doi:10.1029/2011JA017082.

Newell, P. T., and C.-I. Meng (1992), Mapping the dayside ionosphere to the magnetosphere according to particle precipitation characteristics, *J. Geophys. Res.*, *19*(6), 609–612, doi:10.1029/92GL00404.

Newell, P. T., Y. I. Feldstein, Y. I. Galperin, and C.-I. Meng (1996), Morphology of nightside precipitation, *J. Geophys. Res.*, *101*(A5), 10,737–10,748, doi:10.1029/95JA03516.

Newell, P. T., T. Sotirelis, K. Liou, C.-I. Meng, and F. J. Rich (2007), A nearly universal solar wind-magnetosphere coupling function inferred from 10 magnetospheric state variables, *J. Geophys. Res.*, *112*, A01206, doi:10.1029/2006JA012015.

Newell, P. T., T. Sotirelis, and S. Wing (2009), Diffuse, monoenergetic, and broadband aurora: The global precipitation budget, *J. Geophys. Res.*, *114*, A09207, doi:10.1029/2009JA014326.

Rich, F. J., D. A. Hardy, R. H. Redus, and M. S. Gussenhoven (1990), Northward IMF and patterns of high-latitude precipitation and field-aligned currents: The February 1986 storm, *J. Geophys. Res.*, *95*(A6), 7893–7913, doi:10.1029/JA095iA06p07893.

Richmond, A. D., and J. P. Thayer (2000), Ionospheric electrodynamics: A tutorial, in *Magnetospheric Current Systems*, edited by S.-I. Ohtani et al., pp. 131–146, AGU, Washington, D. C., doi:10.1029/GM118p0131.

Semeter, J., T. Butler, C. Heinselman, M. Nicolls, J. Kelly, and D. Hampton (2009), Volumetric imaging of the auroral ionosphere: Initial results from PFISR, *J. Atmos. Sol. Terr. Phys.*, *71*, 738–743, doi:10.1016/j.jastp.2008.08.014, [Special Issue] Advances in high latitude upper atmospheric science with the Poker Flat Incoherent Scatter Radar (PFISR).

Solomon, S. C., and V. J. Abreu (1989), The 630 nm dayglow, *J. Geophys. Res.*, *94*(A6), 6817–6824, doi:10.1029/JA094iA06p06817.

Solomon, S. C., P. B. Hays, and V. J. Abreu (1988), The auroral 6300 å emission: Observations and modeling, *J. Geophys. Res.*, *93*(A9), 9867–9882, doi:10.1029/JA093iA09p09867.

Thayer, J. P., and J. Semeter (2004), The convergence of magnetospheric energy flux in the polar atmosphere, *J. Atmos. Sol. Terr. Phys.*, *66*, 807–824, doi:10.1016/j.jastp.2004.01.035, [Special Issue] Upper Atmosphere Tutorials from the 2001 Joint CEDAR SCOSTEP Meeting.

Vasyliunas, V. M. (1979), Interaction between the magnetospheric boundary layers and the ionosphere, in *Proceedings of the Magnetospheric Boundary Layers Conference, ESA Spec. Publ.*, vol. 148, edited by B. Battrick et al., pp. 387–393, ESA, Paris.

Winningham, J. D., F. Yasuhara, S. I. Akasofu, and W. J. Heikkila (1975), The latitudinal morphology of 10 eV to 10 keV electron fluxes during magnetically quiet and disturbed times in the 2100–0300 MLT sector, *J. Geophys. Res.*, *80*(22), 3148–3171, doi:10.1029/JA080i022p03148.

Wygant, J. R., and A. Keiling (2000), Polar spacecraft based comparisons of intense electric fields and Poynting flux near and within the plasma sheet-tail lobe boundary to UVI images: An energy source for the aurora, *J. Geophys. Res.*, *105*(A8), 18,675–18,692, doi:10.1029/1999JA900500.

Zhang, B., W. Lotko, O. Brambles, S. Xi, M. Wiltberger, and J. Lyon (2014), Solar wind control of auroral Alfvénic power generated in the magnetotail, *J. Geophys. Res. Space Physics*, *119*, 1734–1748, doi:10.1002/2013JA019178.